Design of a 48 GHz Gyroklystron Amplifier

Laurence J. R. Nix, Liang Zhang, and Adrian W. Cross, *Member, IEEE*

***Abstract*— The continued development of linear accelerators at higher frequencies poses several technological challenges. One such challenge is the requirement for high-frequency amplifiers to drive linearization systems. Presented in this article is the design of a 48 GHz gyroklystron amplifier appropriate for application in a harmonic linearizer for a 6 GHz or 12 GHz drive frequency. The beam used in the gyroklystron is provided by a magnetron injection gun (MIG), which has been designed using genetic optimization. The gyroklystron interaction circuit was designed with the aid of a Particle-in-Cell (PIC) simulation study which predicted 2 MW of output power at 48 GHz with a gain of 35 dB and an efficiency of 38%. This article summarizes the preceding work on the interaction circuit and MIG with additional phase stability analysis as well as presenting the design and analysis of vacuum windows, an input coupler, and the collector.**

***Index Terms*— Gyroklystron, magnetron injection gun (MIG), microwave amplifier, particle-in-cell (PIC) simulation, vacuum electronic devices.**

I. Introduction

THE gyroklystron amplifier is a member of cyclotron resonance maser (CRM) mechanism family [1], which also includes gyrotron oscillators and gyro-traveling wave amplifiers. Each of these devices is based on the interaction of a gyrating electron beam with the transverse electric (TE) mode in the interaction circuits.

Historically, most gyroklystron research has related to radar applications [2], [3] and the idea of gyroklystron-driven linear accelerators has also been explored [4]. Although many promising results are summarized in [4] and [5], this line of study did not lead to the use of gyroklystrons as drivers for accelerating cavities and klystrons are still the industry standard. Commercially available klystrons can comfortably deliver the required power at the C-band and X-band drive frequencies which are currently favored in accelerator design [6].

Manuscript received June 18, 2021; revised August 13, 2021; accepted August 25, 2021. This work was supported in part by the European Commission Horizon 2020 Project "CompactLight" under Grant 777431-XLS, in part by the Science and Technology Facilities Council (STFC), U.K., Cockcroft Institute Core under Grant R160525-1, and in part by the U.K. Engineering and Physical Sciences Research Council (EPSRC) under Grant EP/S00968X/1. The review of this article was arranged by Editor D. K. Abe. *(Corresponding author: Laurence J. R. Nix.)*

The authors are with the Department of Physics, SUPA, University of Strathclyde, Glasgow G4 0NG, U.K., and also with The Cockcroft Institute, Warrington WA4 4AD, U.K. (e-mail: laurence.nix@strath.ac.uk; liang.zhang@strath.ac.uk; a.w.cross@strath.ac.uk).

Color versions of one or more figures in this article are available at https://doi.org/10.1109/TED.2021.3108746.

Digital Object Identifier 10.1109/TED.2021.3108746

In high-energy linear accelerators, in order to generate the femtosecond bunches required while maintaining a high bunch charge, a magnetic chicane is typically included for bunch compression. An energy chirp is applied to the bunch before compression. As the path length through the chicane is energy-dependent, the bunch is compressed in time. However, as voltage varies sinusoidally, the chirp is nonlinear in time, and an additional section must be included to linearize the chirp. The most well-developed linearization method is harmonic linearization [7], wherein an additional cavity at a harmonic of the drive frequency is used to flatten the field-profile experienced by the electrons. The frequencies required of the linearizer are high, and conventional klystrons cannot deliver sufficient power. For example, the CompactLight X-ray free-electron laser (XFEL) design study features a 36 GHz (*Ka*-band) linearizer, with a power demand beyond currently available commercial amplifiers at that frequency [8]. Two solutions have been proposed; a multibeam (20 beam) klystron (MBK) [9] and a gyroklystron [10] which show comparable performance with each other and both remain viable options moving forward.

There was also a strong incentive to explore the possibility of a 48 GHz (fourth harmonic) linearizer as the voltage required from the linearizer scales with the inverse square of harmonic number relative to injector frequency. The voltage required for a 48 GHz linearizer was 3.5 MV, compared with 6.2 MV at 36 GHz [11], [12]. Therefore, a higher harmonic option can lower the energy cost of the system.

Respectively, Nix *et al.* [13] and Zhang *et al.* [14] describe the work performed on the interaction circuit and magnetron injection gun (MIG) for this project. This article presents the detailed design of the other components in the gyroklystron, including the input coupler, vacuum windows, and the thermal analysis of the collector region. These components together with the published interaction circuit and the MIG provide a complete design solution of the 2 MW 48 GHz gyroklystron.

II. Principle and Overall Design of Gyroklystron

Fig. 1(a) shows a simple flowchart covering each section of the gyroklystron design. A high-voltage high-power modulator which is available from Scandinova [15] will be used to provide the required beam voltage and current. The high-power microwave radiation extracted through the output window will be fed into the SLAC Energy Development (SLED)-II type pulse compressor (with a power compression ratio of $\sim$7) and used to drive the linearizer [16]. Each of the boxed components

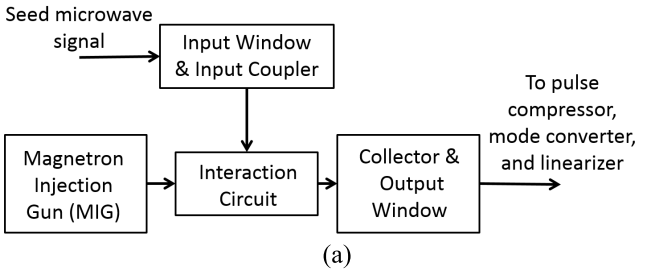

(a)

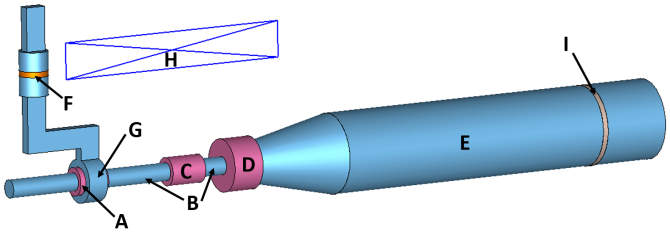

(b)

Fig. 1. (a) Flowchart of the gyroklystron. (b) Components of the gyroklystron design (not to exact scale), cavities highlighted in pink. A–input cavity; B–drift tubes; C–intermediate cavity; D–output cavity; E–collector; F–pillbox-type coupler with input window; G–coaxial input coupler for first cavity; H–solenoid; and I–output window.

in Fig. 1(a) has been studied as part of this work and is presented in the following sections.

High-frequency gyroklystrons are sometimes designed to operate at the second harmonic to lower the magnetic field requirement at the cost of reduced efficiency [17], [18]. In this instance, a fundamental harmonic design was preferred as maximizing efficiency was a primarily goal. Additionally, highly stable operation was desired and magnetic field variations have a lesser impact on a fundamental harmonic device.

Fig. 1(b) shows a 3-D representation of the interaction circuit and input coupler. In the gyroklystron, microwave power is coupled into an input cavity to excite a $TE_{0,1,1}$ mode which applies phase-bunching forces to the electron beam. One or more intermediate cavities serve to reinforce the bunching effect, and then the bunched electrons transfer a portion of their energy to the field in the output cavity. The electron beam is generated by a MIG in which electrons emitted from a thermionic cathode are guided into the beam tunnel with the desired properties by an optimized arrangement of magnetic fields. Since only transverse momentum is lost during the interaction, the beam still has a large amount of power at the point of deposition and the thermal effect on the collector must be considered.

III. MIG and Interaction Circuit

The initial parameters of the MIG were estimated using the Baird tradeoff equations [19]. These estimates were then optimized by the finite element trajectory solver TRAK [20], using a multiobjective genetic algorithm considering 11 geometric and four field parameters. Further detail on the theory and methodology is presented in [14]. The optimized MIG achieved a spread of 8.9% in the transverse-to-axial velocity ratio α. The interaction circuit is a three-cavity configuration,

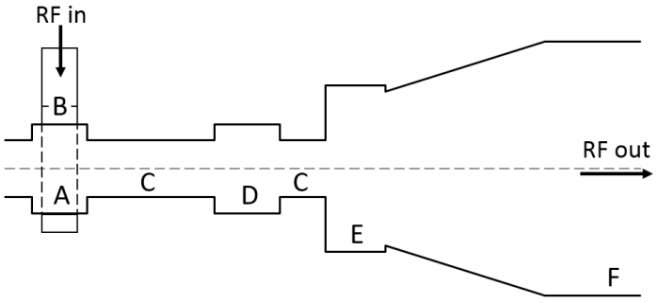

Fig. 2. Schematic of a three cavity gyroklystron interaction circuit. A–input cavity; B–input coupler; C–drift tubes; D–intermediate cavity; E–output cavity; and F–collector.

as shown in Fig. 2. The detailed design process has been presented in [13], summarized as follows.

1) Cavity sizes were estimated through consideration of eigenfrequency equations, cutoff frequency, and coupling coefficients.
2) The initial beam parameters and the estimated gain was obtained using gyroklystron linear theory [21].
3) The linear theory designs were refined using a self-consistent nonlinear model [22], [23].
4) The design was verified and reoptimized using particle-in-cell (PIC) simulation in MAGIC [24], and the performance was tested over various input parameter sets.

The main results described in [13] and [14] show that the gyroklystron's ideal-beam output power is 2.3 MW with a 37 A, 150 kV beam. With the optimized MIG's α-spread of 8.9%, the predicted output power of the gyroklystron is reduced to 2.0 MW. This meets the power requirement of the SLED-II pulse compressor and linearizer design. Confidence in the simulation results is high as MAGIC has been used in the design of several gyroklystron amplifiers and shown good agreement between simulation and experimental data [25]–[27]. The linearizer specification also places the demand that the phase stability of the amplifier should be no higher than 0.5° [11]. This can be calculated by (1) and the detailed derivation is presented in [28]

$$d\phi = \left(1+\alpha^2\right)^{\frac{1}{2}} \frac{\omega L}{c} \frac{\left(\gamma^2-1\right)^{\frac{1}{2}}}{\gamma+1} \left(1+\frac{\Delta}{2}\frac{\alpha^2}{1+\alpha^2}\frac{\alpha^2-\gamma}{\gamma}\right)\frac{dV}{V} \tag{1}$$

where L is the length of the interaction circuit and Δ is the normalized detuning parameter. As most of the parameters in (1) are fixed based on the design of the interaction circuit, the primary influence on phase stability is the voltage stability of the high-power modulator. The phase stability over the device length was calculated to be 0.26° per 0.01% voltage stability of the modulator. Scandinova's K100 modulator can meet extreme stability specifications [15]. Therefore, the designed gyroklystron can meet the requirement of the typical linearizer system for the CompactLight XFEL.

IV. Coaxial Input Coupler

Initial simulations of the interaction circuit simply assume an ideal $TE_{0,1,1}$ mode being excited. In practice, it is not

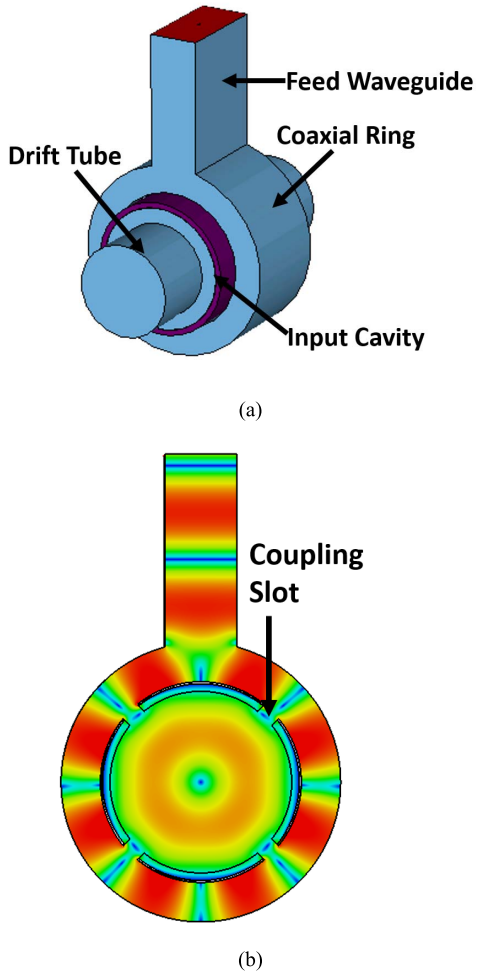

Fig. 3. Coaxial coupler geometry. (a) 3-D model. (b) Cross section with field pattern.

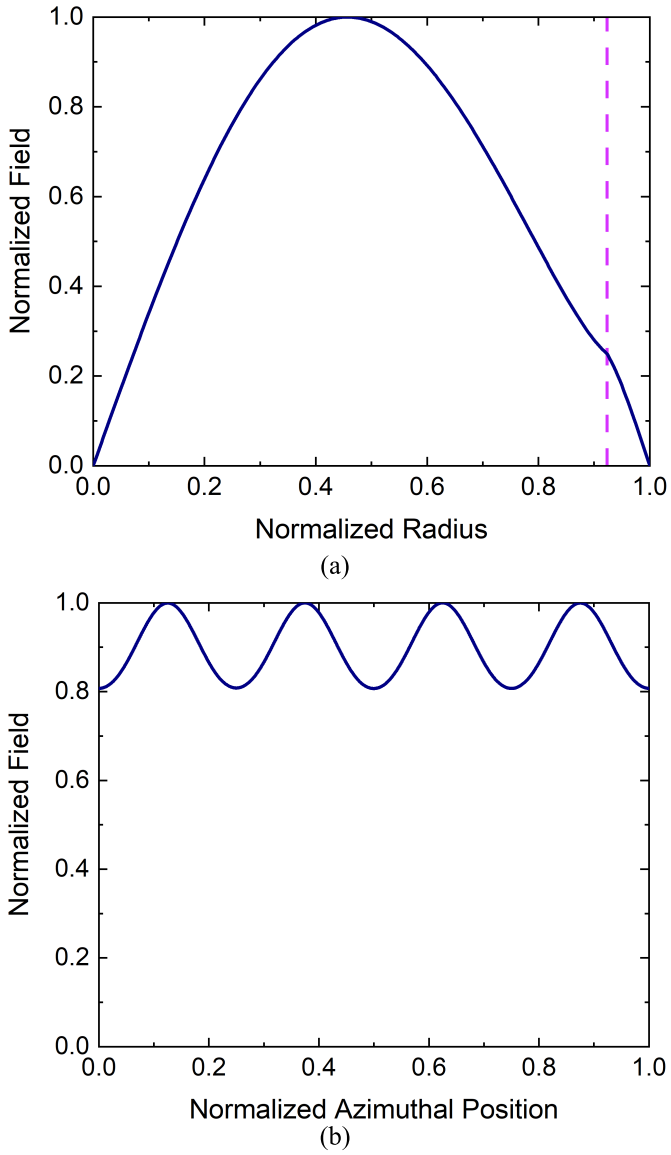

Fig. 4. (a) Radial and (b) azimuthal field-profile in the input coupler. The dashed line in the top figure indicates the beginning of the dielectric wall-lining.

so trivial to excite the correct mode, and the design of the coupling system must be considered as part of the complete gyroklystron design. The seed microwave signal is supplied to the input cavity through a coaxial input coupler of the arrangement shown in Fig. 3.

A rectangular waveguide feeds into a coaxial cavity which encircles the gyroklystron input cavity. Four evenly spaced slots on the shared wall between the gyroklystron cavity and the coaxial ring allow energy to leak through and excite the desired mode.

By this structure, a rectangular $TE_{0,1}$ waveguide mode is converted to a $TE_{4,1,1}$ coaxial cavity mode and then to a $TE_{0,1,1}$ cylindrical cavity mode. The standard WR22 waveguide (5.69 mm $\times$ 2.84 mm) was selected for convenience of manufacture and the cavity dimensions are determined by the optimized interaction circuit [13]. The inner radius of the coaxial section (4 mm) is just larger than the cavity radius accounting for wall thickness. The remaining parameters to consider are therefore the outer radius of the coaxial region and the dimensions of the coupling slots. The outer radius of the coaxial region should be that which sets the eigenfrequency of the coaxial $TE_{4,1,1}$ mode to 48 GHz, which in this case was 5.57 mm. Finite-difference time-domain (FDTD) simulations in CST Microwave Studio were then performed to analyze and optimize for the best achievable mode purity of the $TE_{0,1}$ mode in the input cavity. To demonstrate the feasibility of the design, a simplified model was computed, showing effective excitation of the desired mode in an unlined cavity. The actual cavity requires a dielectric layer on the outer wall to maintain the correct Q of 180. The dielectric properties used in this simulation were $\varepsilon_r = 12$ and $\tan(\delta) = 0.62$, which can be achieved with a BeO:SiC compound [29]. The simulated reflection parameter at the input port was exported and postprocessed with Q factors calculated by the method and program described in [30]. Initial simulations showed that this made it more difficult for the coupler to excite a pure mode. Parameter sweeps over the aperture dimensions were performed to improve mode coupling, resulting in the field-profile shown in Fig. 4. The optimized coupling slots were rectangular with dimensions of 2.3 mm $\times$ 0.8 mm.

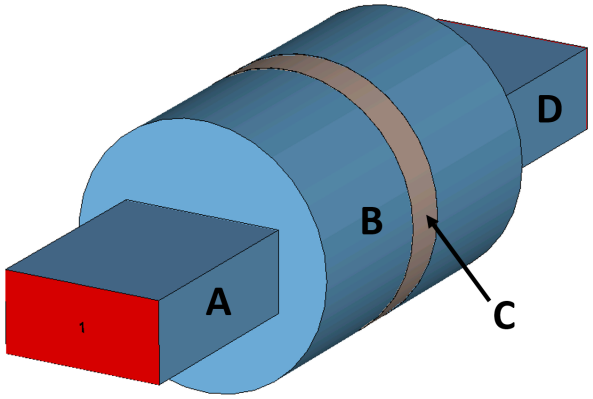

Fig. 5. Geometry of the input window. A–waveguide from microwave source; B–cylindrical pillbox section; C–alumina disk; and D–feed waveguide to the input coupler.

The peak field along the radial line occurs at $0.45r_c$ rather than the optimal $0.48r_c$, though this offset is smaller than both the Larmor radius of electron orbits and the thickness of the beam and is hence not expected to significantly influence the device performance. In the azimuthal direction, the peak field magnitude varies 11% above and below its average value, which can be accounted for by a slight increase in input power to ensure that all electrons receive sufficient accelerating force. To investigate the mode purity, one end of the cavity was widened to allow the coupled wave to propagate into a waveguide structure where its composition was analyzed at an exit port. The output mode was an almost pure $TE_{0,1,1}$ mode and other modes were negligible.

V. Vacuum Windows

The input and output windows of the gyroklystron have been designed. In addition to appropriate physical strength and vacuum sealing, the windows must have reflection coefficients as small as possible over the operating frequency band. Several types of window design exist, but the choice is partly limited by the geometry of the device. In this case, the input coupler (Section IV) features a rectangular waveguide. To avoid the need for additional steps or tapers, a pillbox-type structure [31] was selected for the input window as pictured in Fig. 5. For the output window, a single-disk circular window was selected as this could fit conveniently into the established output waveguide geometry. The rectangular sections of the input window arrangement are identical in dimension to those of the input coupler.

The optimal window thickness depends on the dielectric constant of the material and can be estimated by

$$d = N\left(\frac{\sqrt{\lambda_d}}{2}\right) \tag{2}$$

where N is an integer, and λ_d is the wavelength in the material calculated from the wavelength and relative permeability by

$$\lambda_d = \frac{\lambda}{\sqrt{\varepsilon_r'}}. \tag{3}$$

The choice of window material depends on the thermal, mechanical, and optical properties of the material. In this

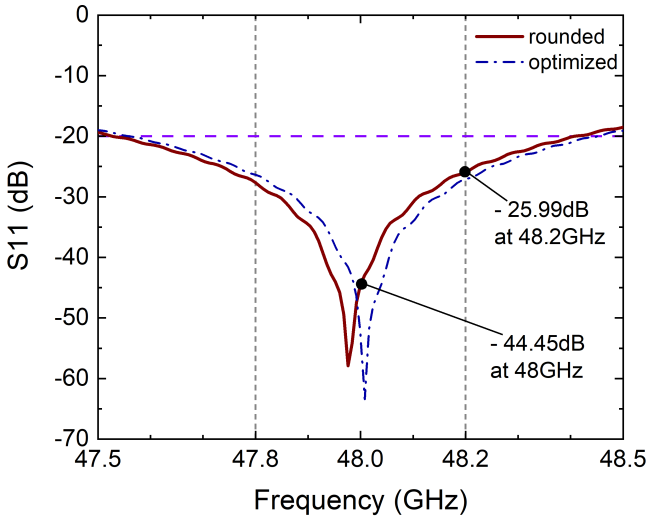

Fig. 6. Reflection parameters of the input window.

case, 95% Al_2O_3 was used, which has a relative permittivity of 9.4.

The radius of the input window's cylindrical section was estimated with consideration of the cutoff frequency. The thickness was estimated (2), but since the device has a bandwidth requirement, it is not as simple as choosing the ideal thickness at 48 GHz. Therefore, the dimensions were optimized in CST Microwave Studio to minimize reflection over the full range of the bandwidth. There is no fixed point that separates good and bad performance, so upper limits were set by the reasonable judgment of a suitable order of magnitude. The limits selected were −35 dB at the center frequency (48 GHz) and −20 dB within the gyroklystron's 3-dB bandwidth (47.8–48.2 GHz). The reflection was shown to be highly sensitive to geometry. An initial optimization sequence only specifying to move the minimum to 48 GHz displayed exceptional reflection of −58 dB at 48 GHz, but failed to meet the target values across the full bandwidth. The optimizer goals were reassessed, and it was instead considered that provided the reflection parameter at 48 GHz met the requirement, the exact position of the minimum value may be allowed to shift. This approach proved successful, as it allowed the maximum value within the specified frequency range to improve from −17 to −26 dB. The reflection at 48 GHz changed to −53 dB, which is still significantly better than the chosen target. A conservative estimate of 10 μm machining precision was assumed. With dimensions rounded to this level, the reflection parameters were −44 dB at 48 GHz and −26 dB within the bandwidth, which is still better than the chosen targets. Fig. 6 illustrates the difference between the optimized and rounded curves. The rounded dimensions were a pillbox radius of 4.64 mm, a pillbox length of 11.10 mm, and a disk thickness of 1.58 mm.

For the single-disk output window, boron nitride (BN) was selected as the window material as it offers excellent mechanical strength and thermal properties, at the same time is much cheaper than CVD diamond. While the high pulse repetition frequency required by the XFEL is high at 1000 Hz with 1.5 μs pulse duration, the average power is much lower

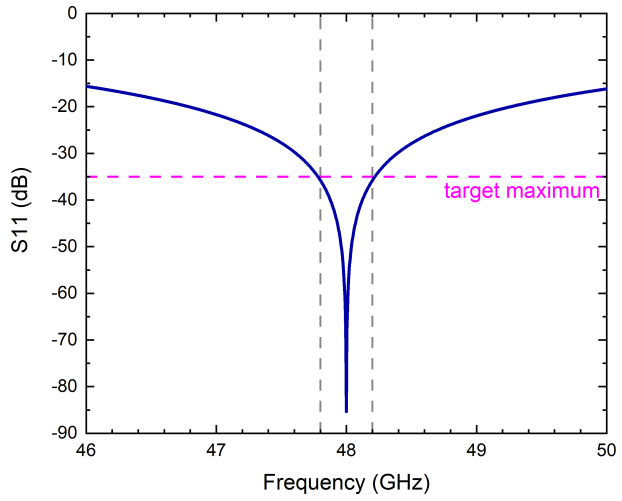

Fig. 7. Reflection curve of the optimized output window, which meets the specified target reflection parameter across the bandwidth.

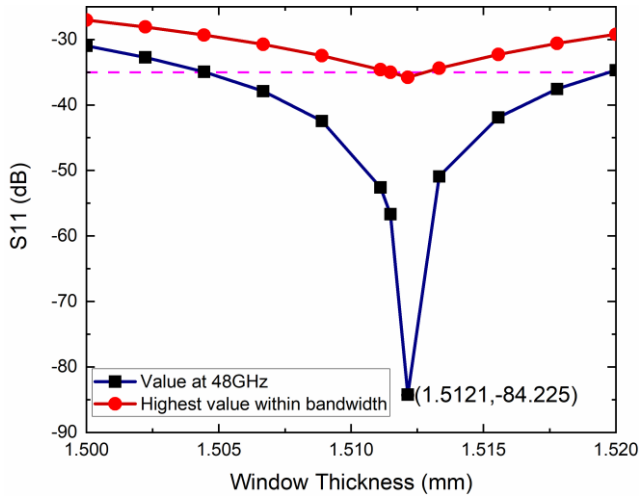

Fig. 8. Variation of reflection parameter of the output window as window thickness is adjusted.

than a continuous wave (CW) device, and therefore a BN window can safely handle the power load. Reflection from the output window poses more risk to the performance than from the input window, as reflections here would travel back toward the interaction region and may interfere with the output mode. A stricter limit of −35 dB reflection was therefore set as the target maximum over the device bandwidth. The reflection curve is illustrated in Fig. 7.

The optimized dimensions displayed a maximum reflection of −36 dB within the bandwidth, but again there was high sensitivity to thickness. Fig. 8 illustrates the tolerance requirement of the window thickness. The optimal window thickness was 1.51 mm.

High machining precision of 10 μm is required to meet the specified target over the bandwidth range, while the value at 48 GHz remains suitably low for a larger thickness range. The true dielectric constant in the manufactured material may also differ from the assumed value slightly. It is therefore possible to construct a window that is slightly thicker than the calculated value and grind it to the correct value after

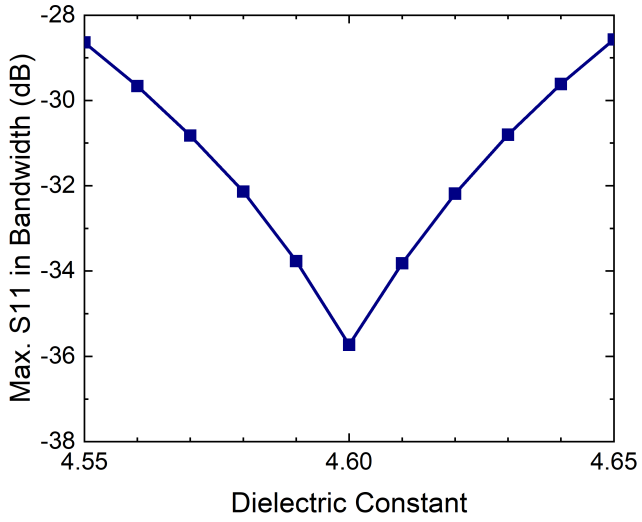

Fig. 9. Variation of reflection parameter of the output window as dielectric constant is adjusted.

measurement using a vector network analyzer. Fig. 9 shows the variation of the maximum reflection within the gyroklystron's 3-dB bandwidth for a range of dielectric constants at a fixed window width.

VI. Collector and Its Thermal Analysis

The optimal interaction efficiency was around 40%, thus leaving around 60% of the beam power present when it is deposited after the interaction. Although the short-pulsed operation leads to a much lower average power than a CW device, the loading is still large enough that thermal analysis and cooling systems are necessary. Here a two-stage process was used. First, the particle data from the PIC simulation was imported into CST's trajectory solver, which was used to calculate the paths of electrons through the collector region and determine deposition density. The trajectory solver result was then imported to CST's thermal analysis program as a heat source. Since the PIC simulations did not fully account for the pulsed operation, the power was reduced by setting a scaling factor on the imported heat source. For 1.5 μs pulses at a repetition rate of 1000 Hz, the scaling factor would be 0.0015. However, that factor assumes perfect square pulses and optimal interaction. It is an important precaution to design around the full beam power. A 2 μs linear rise (and fall) time was taken, though this was a conservative estimate, and a shorter rise is plausible with current modulator technology. The scaling factor used accounting for this rise time and the full beam power was 0.006. The rounding and approximations made in determining the scaling factor all provide a slight upward error, meaning that the simulation result is unlikely to result in underestimating the value.

The deposition heat source is a surface plot with no dependency on the external structure. Preliminary analysis of an 11.6 mm collector showed that peak deposition density would be very high. Minor adjustments to the magnetic field-profile were able to provide only small improvements. Including a tapered section or changing the collector radius increase the surface area of deposition and hence lowers maximum loading.

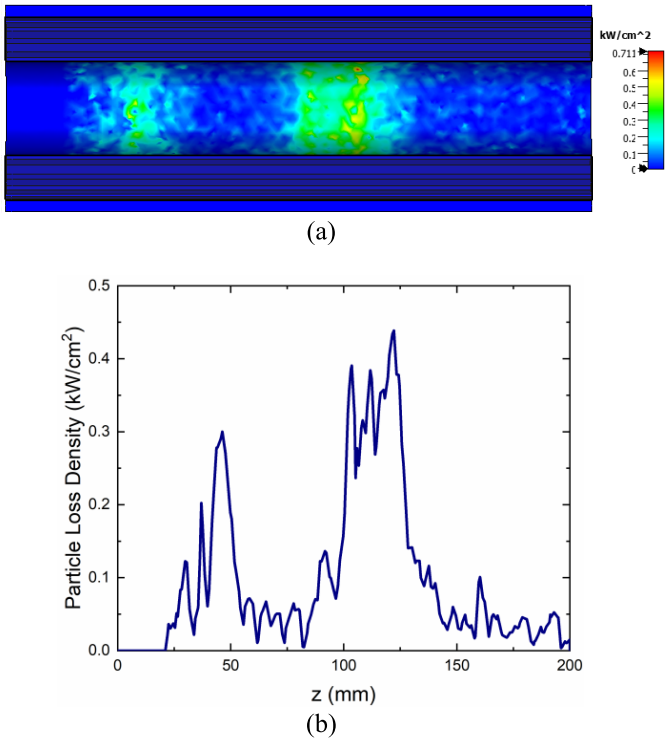

Fig. 10. (a) Particle deposition density on a surface cross section and (b) along an arbitrary surface line in the collector region.

The surface area is maximized when the deposition takes place on a large-radius cylindrical wall. Since the particle import interface is far from the cavity region, there is space for tapering to occur before the deposition region, and safe performance is predicted to be possible with a 16 mm radius cylindrical collector region. Small, localized areas with a peak deposition density of around 0.71 kW/cm^2 were observed as shown in Fig. 10(a), while the vast majority of the surface saw loading under 0.5 kW/cm^2.

Fig. 10(b) shows the particle deposition density along a line following the surface in the axial direction, where $z = 0$ is the position of the import interface for electrons which was placed 140 mm from the output cavity aperture. The deposition is not perfectly symmetrical, but the peaks remain at the same position and roughly the same magnitude whichever line is chosen. Fig. 11 shows the electron trajectories in the collector region and an example temperature plot with a maximum temperature of 120 °C.

The thermal analysis was also considered in the full-beam zero-drive case as the beam profile would differ without bunching effects. The resulting peak temperature and surface loading values on the collector heating were observed to remain at safe levels in the event of input source failure.

A realistic collector typically requires a cooling system to ensure safe operation. The cooling system consists of a pumping system to provide a flow of pressurized cold water to carry heat away from the collector walls [32]–[34]. Grooves are included to increase the surface area of the contact surface between the copper and the water. Fig. 12 shows the groove geometry proposed for the collector structure. In the thermal analysis, the effect of water-cooling was approximated by

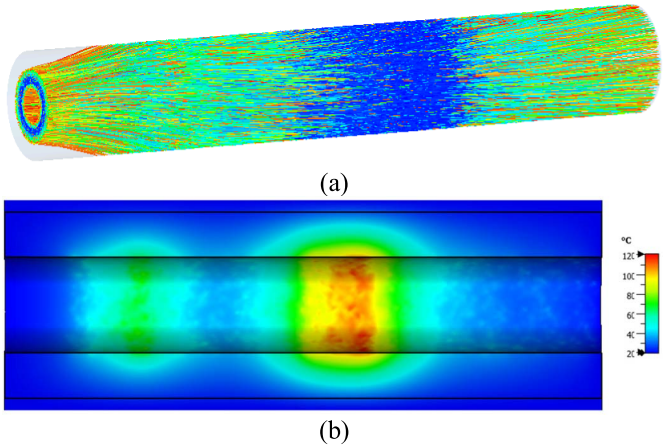

Fig. 11. (a) Electron trajectories and (b) temperature distribution in the collector region.

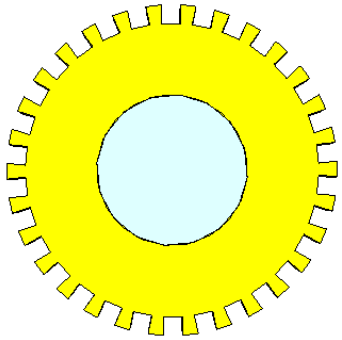

Fig. 12. Cross section of proposed axial groove geometry to increase the surface area of the metal–water interface.

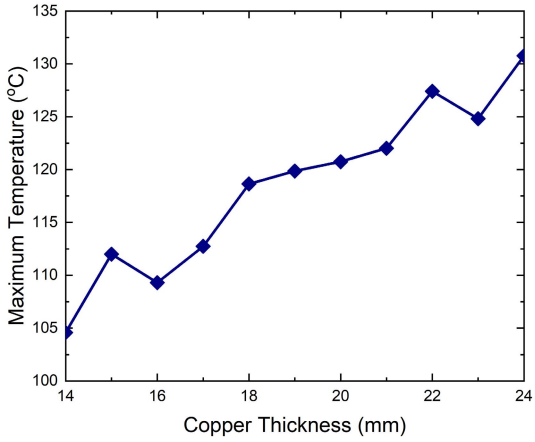

Fig. 13. Variation of maximum temperature with increasing copper thickness.

applying a convective heat transfer coefficient of 3 W/cm^2/K to the surface [35].

If the thickness of copper between the deposition surface and the water-cooling surface is too large, the water cooling is not as effective, but if it is too thin, there is a risk of overheating the water and losing the effect. Hence a parameter sweep was carried out to show the variation of maximum temperature with copper thickness, as shown in Fig. 13. In all cases tested, the peak temperature remains within safe limits for copper and the surface temperature at the metal–water interface remains below boiling point.

Although practical testing would be required to finalize the cooling system design, the results discussed here demonstrate the feasibility of the collector, showing peak temperature and peak deposition density to be safely within the material limits of copper.

VII. Conclusion

In this article, the design of a 48 GHz gyroklystron amplifier has been presented. The preceding results presented in [13] and [14] have been summarized and expanded upon with additional discussion on the phase stability, which has been shown to meet the linearizer requirement if an appropriate modulator is used. The vacuum windows and input coupler have been designed. The input window comfortably met design targets, and the output window can meet design targets provided that the machining precision of the window material is sufficiently high. The input coupler was predicted to excite a $TE_{0,1,1}$ with a slight impurity that caused variations in the peak field by 11% around an azimuthal line. Finally thermal analysis of the beam deposition region was performed, demonstrating that the power loading and peak temperature in a 16-mm radius collector are safe at a very high repetition rate of 1000 Hz. The feasibility of the interaction circuit, MIG, vacuum windows, and collector has been demonstrated through detailed simulation work, and together these components form a viable design for a MW-level 48 GHz gyroklystron suitable for application in a linearizer for an XFEL.

References

[1] J. L. Hirshfield and J. M. Wachtel, "Electron cyclotron maser," *Phys. Rev. Lett.*, vol. 12, no. 19, pp. 533–536, May 1964, doi: 10.1103/PhysRevLett.12.533.

[2] A. A. Tolkachev, B. A. Levitan, G. K. Solovjev, V. V. Veytsel, and V. E. Farber, "A megawatt power millimeter-wave phased-array radar," *IEEE Aerosp. Electron. Syst. Mag.*, vol. 15, no. 7, pp. 25–31, Jul. 2000, doi: 10.1109/62.854021.

[3] G. J. Linde, M. T. Ngo, B. G. Danly, W. J. Cheung, and V. Gregers-Hansen, "WARLOC: A high-power coherent 94 GHz radar," *IEEE Trans. Aerosp. Electron. Syst.*, vol. 44, no. 3, pp. 1102–1117, Jul. 2008, doi: 10.1109/TAES.2008.4655367.

[4] V. L. Granatstein and W. Lawson, "Gyro-amplifiers as candidate RF drivers for TeV linear colliders," *IEEE Trans. Plasma Sci.*, vol. 24, no. 3, pp. 648–665, Jun. 1996, doi: 10.1109/27.532948.

[5] W. Lawson, J. P. Calame, G. S. Nusinovich, and B. Hogan, "Reflections on the university of Maryland's program investigating gyro-amplifiers as potential sources for linear colliders," *THz Sci. Technol.*, vol. 10, no. 1, pp. 1–43, 2017.

[6] D. Sprehn *et al.*, "Latest results in SLAC 75 MW PPM klystrons," *AIP Conf. Proc.*, vol. 807, no. 1, pp. 137–144, 2006.

[7] T. I. Smith, "Production of intense low emittance beams for free electron lasers using electron linear accelerators," *Nucl. Instrum. Methods Phys. Res. A, Accel. Spectrom. Detect. Assoc. Equip.*, vol. 250, no. 1, pp. 64–70, 1986, doi: 10.1016/0168-9002(86)90861-2.

[8] A. Mak, P. Salén, V. Goryashko, and J. Clarke, "XLS deliverable D2.1, WP2: FEL science requirements and facility design," CompactLight Des. Rep., Accessed: May 2021. [Online]. Available: https://www.compactlight.eu/uploads/Main/D2.1_XLS_Specification.pdf

[9] J. C. Cai, I. Syratchev, and G. Burt, "Design study of a high-power Ka-band high-order-mode multibeam klystron," *IEEE Trans. Electron Devices*, vol. 67, no. 12, pp. 5736–5742, Dec. 2020, doi: 10.1109/TED.2020.3028348.

[10] L. Wang *et al.*, "Design of a Ka-band MW-level high efficiency gyroklystron for accelerators," *IET Microw., Antennas Propag.*, vol. 12, no. 11, pp. 1752–1757, 2018.

[11] A. Castilla *et al.*, "Development of 36 GHz RF systems for RF linearisers," presented at the 12th Int. Part. Accel. Conf. (IPAC), Campinas, Brazil, May 2021, Paper FRXB02.

[12] A. Castilla *et al.*, "Studies of a Ka-band lineariser for a compact light source," *Article Submitted Phys. Rev. Accel. Beams*, 2021.

[13] L. J. R. Nix *et al.*, "Demonstration of efficient beam-wave interaction for a MW-level 48 GHz gyroklystron amplifier," *Phys. Plasmas*, vol. 27, no. 5, May 2020, Art. no. 053101, doi: 10.1063/1.5144590.

[14] L. Zhang, L. J. R. Nix, and A. W. Cross, "Magnetron injection gun for high-power gyroklystron," *IEEE Trans. Electron Devices*, vol. 67, no. 11, pp. 5151–5157, Nov. 2020, doi: 10.1109/TED.2020.3025747.

[15] Scandinova. *Product Sheet: K-Series K100*. Accessed: Sep. 2020. [Online]. Available: https://scandinovasystems.com/products/k-series/k100/

[16] P. B. Wilson, Z. D. Farkas, and R. D. Ruth, "SLED II: A new method of RF pulse compression," in *Proc. Linear Accel. Conf.*, 1990, pp. 204–206.

[17] H. W. Matthews *et al.*, "Experimental studies of stability and amplification in a two-cavity second harmonic gyroklystron," *IEEE Trans. Plasma Sci.*, vol. 22, no. 5, pp. 825–833, 1994, doi: 10.1109/27.338298.

[18] S. X. Xu *et al.*, "A Ka-band second harmonic gyroklystron amplifier," *IEEE Trans. Plasma Sci.*, vol. 40, no. 8, pp. 2099–2104, Aug. 2012, doi: 10.1109/TPS.2012.2199522.

[19] J. M. Baird and W. Lawson, "Magnetron injection gun (MIG) design for gyrotron applications," *Int. J. Electron.*, vol. 61, no. 6, pp. 953–967, 1986, doi: 10.1080/00207218608920932.

[20] S. Humphries, Jr., "Numerical modeling of space-charge-limited charged-particle emission on a conformal triangular mesh," *J. Comput. Phys.*, vol. 125, no. 2, pp. 488–497, May 1996, doi: 10.1006/jcph.1996.0110.

[21] G. S. Nusinovich, B. G. Danly, and B. Levush, "Gain and bandwidth in stagger-tuned gyroklystrons," *Phys. Plasmas*, vol. 4, no. 2, pp. 469–478, Feb. 1997, doi: 10.1063/1.872115.

[22] M. S. Chauhan, M. V. Swati, and P. K. Jain, "Design and simulation of a gyroklystron amplifier," *Phys. Plasmas*, vol. 22, Mar. 2015, Art. no. 033111.

[23] T. M. Tran, B. G. Danly, K. E. Kreischer, J. B. Schutkeker, and R. J. Temkin, "Optimization of gyroklystron efficiency," *Phys. Fluids*, vol. 29, no. 4, pp. 1274–1281, 1986, doi: 10.1063/1.865876.

[24] B. Goplen, L. Ludeking, D. Smith, and G. Warren, "User-configurable MAGIC for electromagnetic PIC calculations," *Comput. Phys. Commun.*, vol. 87, nos. 1–2, pp. 54–86, May 1995, doi: 10.1016/0010-4655(95)00010-D.

[25] J. J. Choi *et al.*, "Experimental investigation of a high power, two-cavity, 35 GHz gyroklystron amplifier," *IEEE Trans. Plasma Sci.*, vol. 26, no. 3, pp. 416–425, Jun. 1998, doi: 10.1109/27.700773.

[26] M. S. Chauhan, M. V. Swati, and P. K. Jain, "PIC simulation study of a 35 GHz, 200 kW gyroklystron," *J. Microw. Optoelectron. Electromagn. Appl.*, vol. 12, no. 2, pp. 353–362, Dec. 2013.

[27] W. He, C. R. Donaldson, L. Zhang, K. Ronald, A. D. R. Phelps, and A. W. Cross, "Broadband amplification of low-terahertz signals using axis-encircling electrons in a helically corrugated interaction region," *Phys. Rev. Lett.*, vol. 119, no. 18, Oct. 2017, Art. no. 184801, doi: 10.1103/PhysRevLett.119.184801.

[28] G.-S. Park, V. L. Granatstein, P. E. Latham, C. M. Armstrong, A. K. Ganguly, and S. Y. Park, "Phase stability of gyroklystron amplifier," *IEEE Trans. Plasma Sci.*, vol. 19, no. 4, pp. 632–640, Aug. 1991, doi: 10.1109/27.90329.

[29] J. P. Calame and D. K. Abe, "Applications of advanced materials technologies to vacuum electronic devices," *Proc. IEEE*, vol. 87, no. 5, pp. 840–864, May 1999, doi: 10.1109/5.757257.

[30] D. Kajfez, *Q Factor Measurements Using MATLAB*. Norwood, MA, USA: Artech House, 2011.

[31] L. Zhang, C. R. Donaldson, A. W. Cross, and W. He, "A pillbox window with impedance matching sections for a W-band gyro-TWA," *IEEE Electron Device Lett.*, vol. 39, no. 7, pp. 1081–1084, Jul. 2018, doi: 10.1109/LED.2018.2834859.

[32] L. Savoldi *et al.*, "Towards the optimization of the thermal–hydraulic performance of gyrotron collectors," *Fusion Eng. Des.*, vol. 100, pp. 120–132, Nov. 2015, doi: 10.1016/j.fusengdes.2015.04.044.

[33] Y. Shen, W. Jiang, H. Fu, and Y. Luo, "Thermal-hydraulic design of collector cooling for high power gyro-TWT," in *Proc. Int. Conf. Microw. Millim. Wave Technol. (ICMMT)*, May 2018, pp. 1–3.

[34] R. Yan, D. Wang, H. Li, M. Mu, Y. Lian, and Y. Luo, "Design of collectors for high average/continuous-wave power gyro-devices," *IEEE Trans. Electron Devices*, vol. 66, no. 3, pp. 1512–1518, Mar. 2019, doi: 10.1109/TED.2018.2889722.

[35] K. Dong, R. Yan, and Y. Luo, "Optimal design and thermal analysis of undepressed collectors for 35-GHz gyro-TWTs," *IEEE Trans. Electron Devices*, vol. 62, no. 8, pp. 2652–2656, Jun. 2015.